Results of optical monitoring of 5 SDSS double QSOs with the Nordic Optical Telescope

Danuta Paraficz[1], Jens Hjorth[1], and Árdís Elíasdóttir[1,2]

[1] Dark Cosmology Centre, Niels Bohr Institute, University of Copenhagen, Juliane Maries Vej 30, DK-2100 Copenhagen, Denmark
    e-mail: danutas@dark-cosmology.dk
[2] Department of Astrophysical Sciences, Princeton University, Princeton, NJ08544, USA

ABSTRACT

We present optical R-band light curves of five SDSS double QSOs (SDSS J0903+5028, SDSS J1001+5027, SDSS J1206+4332, SDSS J1353+1138, SDSS J1335+0118) obtained from monitoring at the Nordic Optical Telescope (NOT) between September 2005 and September 2007. We also present analytical and pixelated modeling of the observed systems. For SDSS J1206+4332, we measured the time delay to be $\Delta\tau = 116^{+4}_{-5}$ days, which, for a Singular Isothermal Ellipsoid model, corresponds to a Hubble constant of 73^{+3}_{-4} km s^{-1} Mpc^{-1}. Simultaneous pixeleted modeling of five other systems for which a time delay has now been previously measured at the NOT leads to $H_0 = 61.5^{+8}_{-4}$ km s^{-1} Mpc^{-1}. Finally, by comparing lightcurves of the two images of each system, suitably shifted by the predicted or observed time-delays, we found no evidence for microlensing variability over the course of the monitoring period.

Key words. gravitational lensing, cosmological parameters – quasars: individual: SDSS J0903+5028, SDSS J1001+5027, SDSS J1206+4332, SDSS J1353+1138, SDSS J1335+0118

1. Introduction

A gravitationally lensed quasar is a quasar (QSO) which is lensed by a massive foreground object such as a galaxy or a group of galaxies. If the lens is close enough to the line of sight then the quasar is strongly lensed and will be multiply imaged. Due to the different travel times for each light path, any intrinsic variation of the quasar is observed in the images at different times. This time difference, referred to as the time delay, can be measured by comparing the light curves of the images. As first shown by Refsdal (1964) the Hubble constant can be determined from the time delay provided that the mass distribution is known. Conversely, for a fixed Hubble constant, the mass distribution of the lensing galaxy can be constrained.

Determining the Hubble constant from the time delays between light variations in multiple images of gravitationally lensed QSOs is a classical application of lensing in cosmology, but despite 25 years of effort, results remain inconclusive. This is partly due to incomplete knowledge of the mass distribution along the light path to the QSO and partly due to the perturbing effects of microlensing on sparsely sampled light curves of the underlying long-term variations.

To address these issues, we have conducted a monitoring program at the Nordic Optical Telescope (NOT) with the aim of obtaining densely sampled light curves of five lensing systems (SDSS J0903+5028, SDSS J1001+5027, SDSS J1206+4332, SDSS J1353+1138, SDSS J1335+0118). Dense sampling is required to quantify the effects of microlensing (Paczyński 1986; Schild 1996; Paraficz et al. 2006) and to maximize chances of determining a time delay from a relatively short monitoring campaign.

Estimating the Hubble constant using time delay measurements is strongly dependent on the underlying mass distribution and hence the choice of lens model (Oguri 2007). Two different approaches to modeling lenses are commonly used. The first one, the non-parametric method (Saha & Williams 1997), generates a large number of models which perfectly fit the data, each of them gives a different time delay which can be then averaged. For the second method, the analytical method(Keeton 2001), one assumes physical properties of the mass distribution of the lens. Comparison of the two approaches gives a useful indication on the systematic errors in e.g. the Hubble constant determined this way.

Luckily, it seems that simple lens models are very good first approximations to the real mass distributions of lenses (Koopmans et al. 2006). Therefore we have chosen to use the singular isothermal potential to analytically model all the lenses we observe.

In this paper we present the results of a monitoring campaign at the NOT of 5 doubly lensed quasars. We have measured the time delay of one of the lensing systems, SDSS J1206+4332, by analyzing light curves of the two quasar images obtained from six months of monitoring, demonstrating the feasibility of short-term monitoring for time-delay measurement. Based on our measurement of the time delay and 5 other time delay measurements previously obtained at the NOT we have estimated the Hubble constant.

Section 2 describes the details of our monitoring campaign and section 3 introduces the observed targets. The photometric technique based on image deconvolution is described in section 4 and the light curves of all 5 targets are presented in section 5. In section 6 the time delay of SDSS J1206+4332 is determined. In section 7 we perform a microlensing search in the 5 quasar light curves and estimate upper limits to the microlensing signal. In section 8 we perform analytical and pixeleted modeling. Section 9 is devoted to simultaneous modeling of 5 NOT-determined time delay systems with the aim of a joint Hubble constant estimate. In section 10 we discuss the results.

In the paper we use a flat ΛCDM Universe, $\Omega_m = 0.3$ and $\Omega_\Lambda = 0.7$.

2. Observation

The observations were gathered from monitoring programs carried out in the periods September–March 2005/2006, October–March 2006/2007 and April–September 2007 at the Nordic Optical Telescope (NOT); a 2.5-m telescope located at Roque de los Muchachos in La Palma, Spain. The advantage of this telescope is its fairly flexible scheduling, which made almost nightly monitoring possible. Our targets were observed every night under all three operative modes at the NOT: observer, service and technical. However there were severe obstacles preventing frequent sampling: bad weather, Guaranteed Time programs at the NOT and sensitivity of the deconvolution software to imperfectness of the data.

The detectors used in the monitoring were chosen in order to obtain the most frequent sampling and the best image quality. Thus, we used ALFOSC (The Andalucia Faint Object Spectrograph and Camera; pixel scale $0\rlap{.}''189$) whenever it was mounted on the telescope and StanCam (the Stand-by CCD Camera, which is permanently mounted at the NOT; pixel scale $0\rlap{.}''176$), otherwise. The seeing varied from $0\rlap{.}''4$ to $3\rlap{.}''0$ with $1\rlap{.}''0$ being the most frequent value.

We observed the objects in the R band, only. The pilot phase of the program involved monitoring of a gravitationally lensed system SDSS J0903+5028 at $z = 3.6$ (Johnston et al. 2003) for 10 minutes every night. This system contains two quasar images (see Table 3.1) separated by $2\rlap{.}''8$ and aligned on opposite sides of the lensing galaxy at the redshift $z = 0.388$ (Johnston et al. 2003).

After the first observing season we decided to observe three lensed systems alternately, SDSS J1001+5027 and SDSS J1206+4332 together in one night for 5 minutes each, and SDSS J0903+5028 every second night for 10 minutes. The third observing season was again divided in two groups. We continued observing SDSS J1001+5027 and SDSS J1206+4332 for 5 minutes each every second night, alternately with two new targets, SDSS J1335+0118 (5 min) and SDSS J1353+1138 (3 min). The exposure times were chosen so that the signal-to-noise ratio of the fainter component of each system would be above 10. Finding charts of all the targets are presented in Figures 1 and 2.

One of the major challenges in monitoring gravitationally lensed quasars is the lack of prior knowledge of time delay. Thus, time-delay measurements require well-sampled light curves with accurate photometry over a period of time substantially longer than the time delay. Because the time delay is not known, one has to calculate a theoretical time delay before planning the observations.

Assuming that the theoretical prediction of the time delay for a given system is a good approximation (which is not always the case) there is still a question as to whether the quasar will vary during the period of monitoring and what will be the timescale and amplitude of the variations. Quasar brightness might vary from a day up to years independently of the mass of the black hole (Wold et al. 2007). We know that the rapid variability implies a light source at very small distance from the black hole (Webb & Malkan 2000), while variations on long time-scales are related to morphological changes of jets on parsec scales or to accretion-disk instabilities (de Vries et al. 2006). However, it is impossible to predict whether a quasar will vary or not within a given period and timescale, which is why the success of each quasar monitoring is uncertain.

Another difficulty with gravitationally lensed quasar observations is microlensing by stars in the lensing galaxy. Microlensing can change the results by about $0.5 - 1.0$ magnitudes and it is completely unpredictable (Chang & Refsdal 1979).

Thus, in order to get a time delay one has to monitor quasars with high sampling, so that events like microlensing can be extracted from the quasar variability in further analysis. Our monitoring program was designed to minimize this problem.

Observation planning, monitoring supervision and image reduction was made by the first author during her stay at the NOT. Data reduction was performed using IRAF reduction utilities.

3. Targets

The individual targets observed are introduced below. The astrometry and redshifts of the quasar images and the lenses are summarized in Table 3.1.

3.1. SDSS J0903+5028

SDSS J0903+5028, a doubly lensed quasar system, was discovered from the Sloan Digital Sky Survey by Johnston et al. (2003). Using the ARC 3.5 meter telescope it was found that the system has two quasar images separated by $2\rlap{.}''8$ with the lens, a red galaxy ($z = 0.388$), in between. Spectroscopic follow up observation at the Keck II telescope proved that the two objects are the images of one quasar at $z = 3.6$. Johnston et al. (2003) concluded that other galaxies in the vicinity of the lensing galaxy might be gravitationally bound with the lens, adding external shear to the lensed system.

3.2. SDSS J1001+5027 & SDSS J1206+4332

SDSS J1001+5027 and SDSS J1206+4332 were recognized as lensing candidates in a strong lensing survey using the Sloan Digital Sky Survey. Oguri et al. (2005) photometrically and spectroscopically confirmed using the ARC 3.5 meter and University of Hawaii 2.2-meter telescopes, that those two targets are indeed lensing systems. They reported that SDSS J1001+5027 and SDSS J1206+4332 have image separation of $2\rlap{.}''86$ and $2\rlap{.}''90$ respectively with the source objects being quasars at $z = 1.838$ and $z = 1.789$.

Oguri et al. (2005) noted that the two lensing galaxies of SDSS J1001+5027 have colors consistent with those of early-type galaxies at $0.2 \leq z \leq 0.5$. SDSS J1206+4332 appears to have three lensing galaxies where the main lens, G1, has an associated absorber at redshift $z = 0.748$, the second galaxy, G2, is identifed as a high redshift galaxy $z \leq 0.7$ and, the third galaxy, G3, is a blue galaxy. Oguri et al. (2005) using the *lensmodel* software (Keeton 2001) modeled the two systems showing that they are both strongly affected by the potential of more than one galaxy.

3.3. SDSS J1335+0118

SDSS J1353+1138 is a doubly lensed system, discovered in the Sloan Digital Survey by Oguri et al. (2004). The photometric follow up made at the Subaru 8.2-m and Keck I telescopes confirmed that the system consists of two gravitationally lensed images separated by $1\rlap{.}''56$ with a single lensing galaxy in the centre. Spectroscopic observations made at the ESO New Technology Telescope (NTT) showed that the A and B compo-
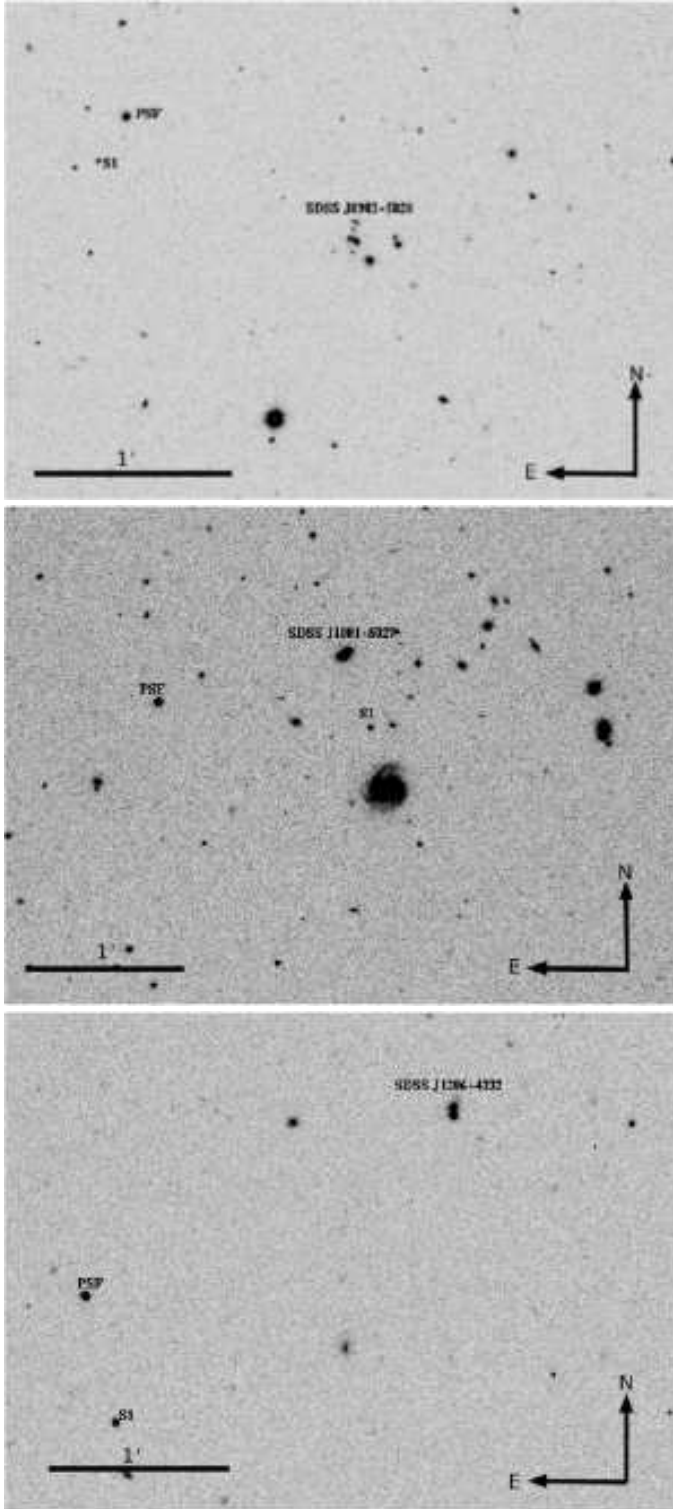
Fig. 1. Finding chart of the three systems: **Top**: SDSS J0903+5028, **Middle**: SDSS J1001+5027, **Bottom**: SDSS J1206+4332. The reference star (S1) and the star used to model the PSF are indicated.

Object	R.A. (J2000.0)	Dec. (J2000.0)	z
SDSS J0903+5028
A	09 03 35.13	+50 28 20.21	3.6
B	09 03 34.88	+50 28 18.75	3.6
G	09 03 34.93	+50 28 19.53	0.388

| SDSS J1001+5027 |
Object	R.A. (J2000.0)	Dec. (J2000.0)	z
A	10 01 28.61	+50 27 56.9	1.838
B	10 01 28.35	+50 27 58.5	1.838
	x[arcsec]	y[arcsec]	z
G1	1.779 ± 0.049	0.857 ± 0.123	$0.2 \leq z \leq 0.5$
G2	1.795 ± 0.088	−0.700 ± 0.053	$0.2 \leq z \leq 0.5$

| SDSS J1206+4332 |
Object	R.A. (J2000.0)	Dec. (J2000.0)	z
A	12 06 29.65	+43 32 17.6	1.789
B	12 06 29.65	+43 32 20.6	1.789
	x[arcsec]	y[arcsec]	z
G1	−0.664 ± 0.137	1.748 ± 0.028	0.748
G2	1.320 ± 0.147	5.999 ± 0.148	≥ 0.7
G3	+2.052 ± 0.200	2.397 ± 0.152	blue

| SDSS J1335+0118 |
	x[arcsec]	y[arcsec]	z
A	0.000 ± 0.001	0.000 ± 0.001	1.57
B	−1.038 ± 0.002	−1.165 ± 0.002	1.57
G	−0.769 ± 0.011	−0.757 ± 0.011	0.44

| SDSS J1353+1138 |
	R.A. (J2000.0)	Decl. (J2000.0)	z
A	13 53 06.35	+11 38 04.81	1.63
B	13 53 06.08	+11 38 01.43	1.63
G	13 35 06.10	+11 38 00.39	∼ 0.3

Table 1. Astrometric properties and redshifts of the five lensed SDSS quasars: SDSS J0903+5028 from Johnston et al. (2003), SDSS J1001+5027 and SDSS J1206+4332 from Oguri et al. (2005), SDSS J1335+0118 from Oguri et al. (2004) and SDSS J1353+1138 from Inada et al. (2006). Units of R.A. are hours, minutes and seconds, and units of Dec. are degrees, arcminutes, and arcseconds. All x,y positions are relative to the A component and their errors do not include the error of the image scale. The positive direction of the those coordinates are to the west and north, respectively.

3.4. SDSS J1353+1138

Inada et al. (2006) discovered the SDSS J1353+1138 lensed quasar system from SDSS lensed quasar survey. For imaging and spectroscopy Inada et al. (2006) used the University of Hawaii 2.2-m telescope, the Keck I and II telescopes and the Magellan Consortium's Landon Clay 6.5-m telescope. The observations showed that the two quasar components separated by 1″41 have redshift $z = 1.629$ and the lensing galaxy in between the images is at $z \sim 0.3$.

4. Photomery and image deconvolution

4.1. Image deconvolution

Time delay estimation requires high precision photometry separately for each lensing image. Since our targets are small angular separation systems we need to use a mathematical method, deconvolution, to separate the images.

An observed image is a convolution of a real light distribution with the so-called total blurring function or point spread function (PSF). The goal of the deconvolution is to extract the brightness of a source using knowledge about the PSF. Deconvolution is an inverse problem without a unique solution.
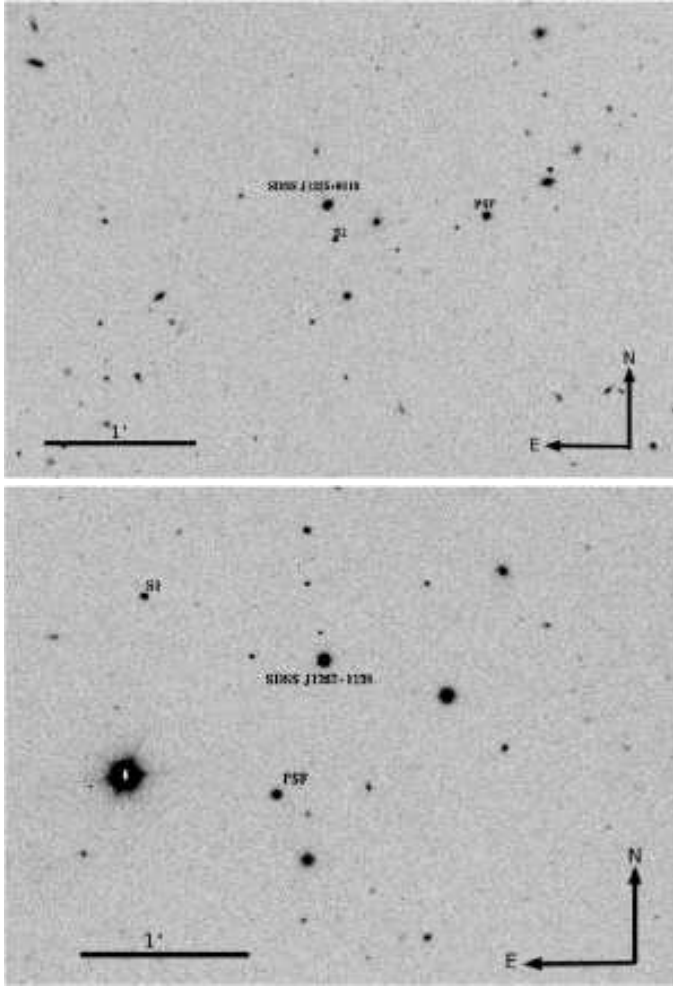
nents of the system are images of a quasar at redshift $z = 1.57$. Eigenbrod et al. (2006b) reported that the lensing galaxy is a low-redshift galaxy with $z = 0.44$.

Fig. 2. Finding chart of the two systems: SDSS J1335+0118 and SDSS J1353+1138. The reference star and the star used to model the PSF are indicated

The method used for choosing the best solution is minimization of the difference between a model and a real image.

All data used in this paper were deconvolved using the PSF Controled Deconvolution software created by Magain et al. (1998). In this software the input are the position and intensities of the images, which need to be well defined to succeed. We take the image positions from previous studies because these were better resolved and the quasar postions well determined (see Table 3.1).

In Figure 3 we present the deconvolution results for the observed targets. On the left are shown the deconvolved images (mathematical models of lensing systems) and on the right the data images. We can see that the deconvolution reveals not only the quasar images but also the lensing galaxies which are not visible in the raw data.

4.2. Photometry

Photometry of all objects presented in this paper was made using the PSF Controled Deconvolution software (Magain et al. 1998). The software deconvolves all frames of a given object simultaneously, it constrains the position of the images and lensing galaxies and allows the magnitude of the quasar images to vary freely. The algorithm has been implemented in various analysis of quasars (Burud et al. 2000, 2002a,b; Hjorth et al.
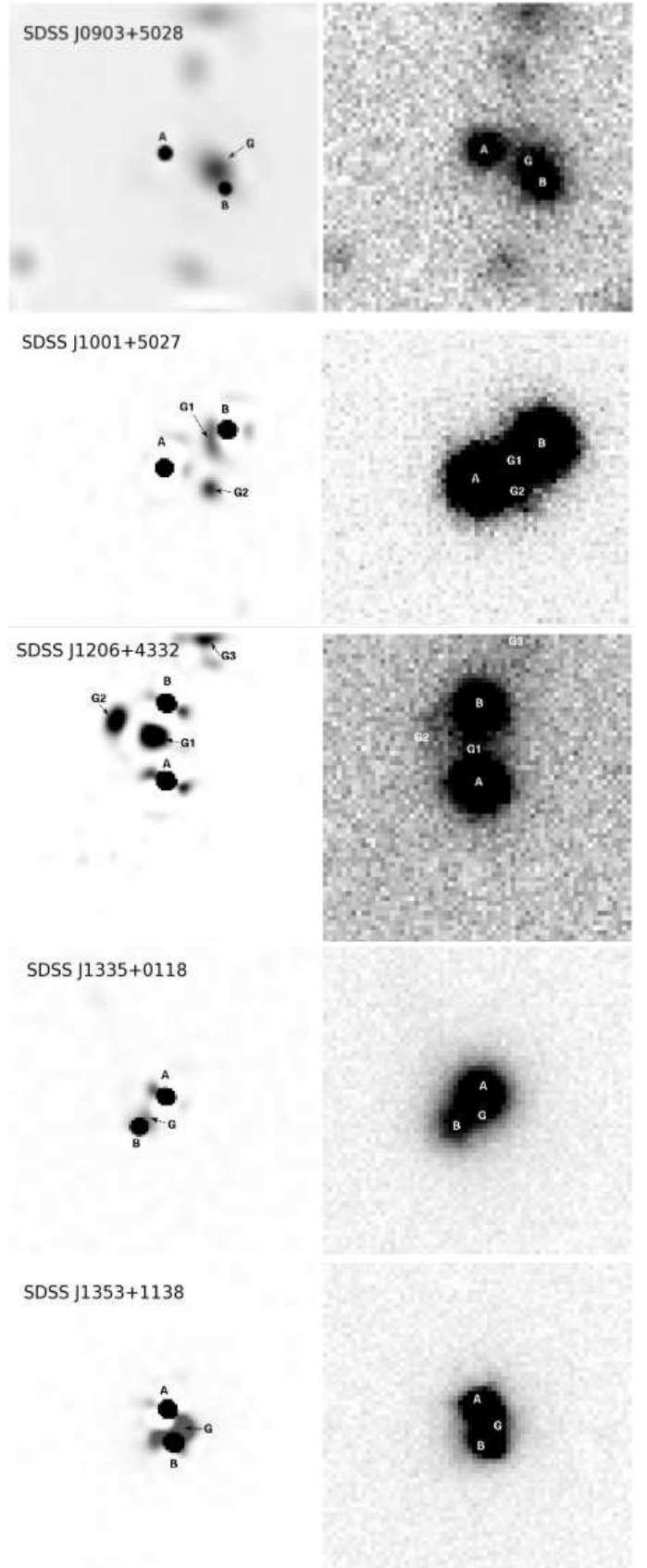

Fig. 3. Results of the deconvolution of the 5 systems. On the left are deconvolved images and on the right original images. The deconvolution reveals not only quasar images but also the lensing galaxy which is otherwise not visible.

2002; Jakobsson et al. 2005; Vuissoz et al 2007; Eigenbrod et al. 2006a).

The light curves of SDSS J0903+5028, SDSS J1335+0118, SDSS J1353+1138, SDSS J1001+5027, SDSS J1206+4332 consist of 34, 31, 31, 24, 34 R-band data points, respectively, as presented in Figures 4-8. Data were taken from two optical cameras, ALFOSC (marked in black) and StanCam (marked in blue). The magnitudes are calculated relative to the PSF magnitude marked on the finding charts (Figures 1 and 2). Due to the small field of view and comparatively small sensitivity of StanCam and lack of bright stars next to our targets the reference stars presented in the plots are only from ALFOSC. The reference star images were also deconvolved to look for systematic errors in the deconvolution and to estimate the photometric uncertainties. Assuming that reference stars are not intrinsically variable any variability seen in their light curves must be due to photometric and deconvolution uncertainties. The error bars of the quasar images and the reference stars coming from ALFOSC are the averaged photon noise and uncertainties measured from the variations of the reference stars combined in quadrature. For data points from StanCam we have assumed one standard error bar of 0.02 mag which should approximately include all uncertainties. In the case of ALOSC data of SDSS J0903+5028 and StanCam data of SDSS J1335+0118 there were no non-variable star in the field except PSF star, thus the error bars of the quasar magnitude are set to 0.02 mag., which is the approximate photometric uncertainty of the B image in average atmospheric conditions.

5. Light curves

5.1. QSOs with little variability

In 3 of the 5 systems (SDSS J0903+5028, SDSS J1335+0118, SDSS J1353+1138) no significant variability was observed. In Figures 4, 5 and 6 we plot the light curves of the three systems. By visual examination we see no variability in the quasar images.
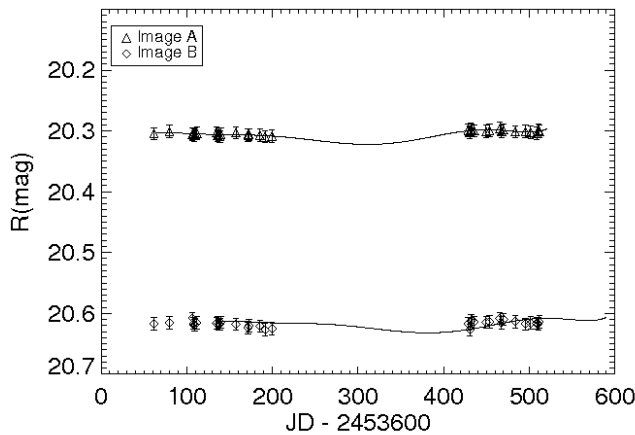

Fig. 5. R-band light curves of SDSS J1335+0118. A (diamonds) and B (triangles) images of the quasar are plotted with black and blue colors indicating weather data coming from ALFOSC or StanCam. The reference star is plotted with red squares. A polynomial is fitted to the A counterpart of the quasars light curve. This polynomial is also fitted to the B image with magnitude and time shift. The time shift is taken from the theoretical prediction of the time delay of this system (see Table 5).

B light curves with magnitude and time shift. Since there are no visible peaks in either light curves, the magnitude shift was chosen simply by taking a difference between average magnitude of image A and image B. The time shift is taken from the theoretical prediction of the time delay of those systems (see Section 8). The fitted polynomials do not show any preferred time shift. This means that due to the lack of quasar variability during the time span of the monitoring we did not manage to measure time delays in these systems.

Fig. 4. R-band light curves of SDSS J0903+5028. A polynomial is fitted to the light curve of A counterpart. This polynomial was also fitted to the B image with magnitude and time shift (see Table 2).

In order to see whether small fluctuations in the light curves say something about the time delay we fitted polynomials to the light curves of the A counterpart. These were then fitted to the
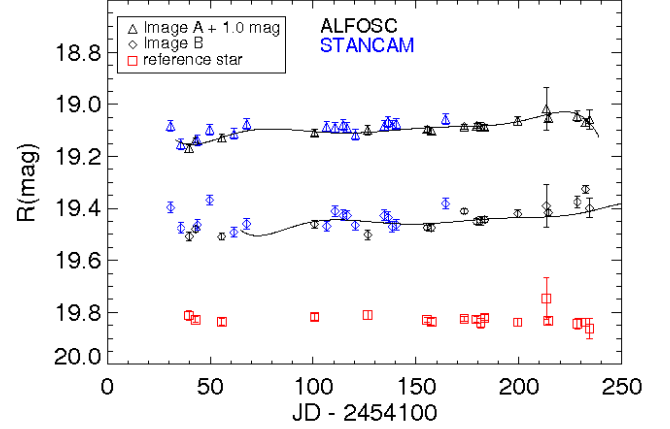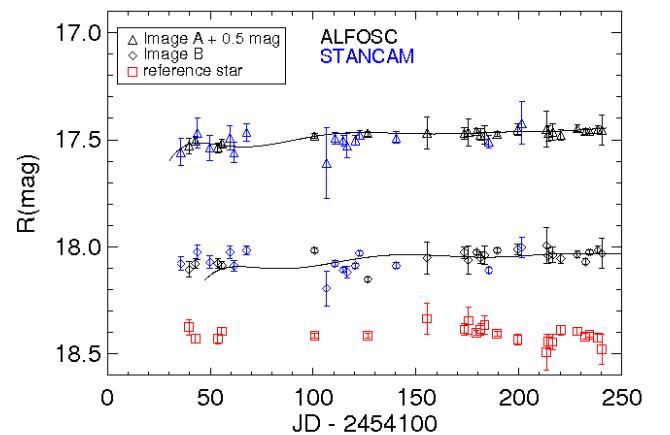

Fig. 6. R-band light curves of SDSS J1353+1138. Shapes and colors of the data point and fitting procedure identical with previous light curve. The time shift is taken from the theoretical prediction of the time delay of those systems (see Table 6).

5.2. Quasars with variability

In 2 out of the 5 monitored gravitationally lensed quasars variability was detected. In Figures 7 and 8 we show the light curves of SDSS J1001+5027 and SDSS J1206+4332, respectively.

5.2.1. SDSS J1001+5027

Figure 7 shows the light curves of SDSS J1001+5027 quasar images. We see that both images have some small variabilities in the light curve and also that both the A and B images have steadily decreased their brightness.
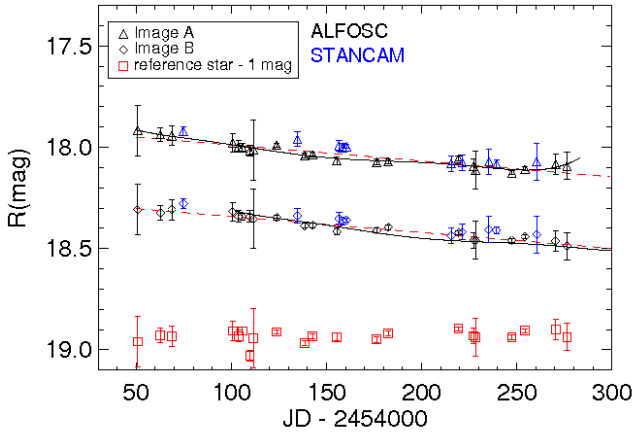

Fig. 7. R-band light curves of SDSS J1001+5027. Polynomials (solid, black lines) and linear regressions (dashed, red lines) are fitted to the A and B counterpart of the quasars separately. Shapes and colors of data point identical as described on previous plots.

We have fitted a 7th order polynomial (see Figure 7 - black solid line) to the A data set. This was then fitted to the B light curve with magnitude shift which is the average magnitude difference between light curves (0.4 mag) and time shift which is the predicted time delay (52 days).

We also have fitted a straight line to light curves (see Figure 7 – red dashed lines). The linear regression shows that both light curves have very similar evolution. Both images decreased their brightness by 0.2 magnitude during the first 200 days. This indicates that the brightness decrease is due to long intrinsic quasar variability (de Vries et al. 2003).

Although variability is clearly visible, it is impossible to measure the time delay for this system just from the slope. The small fluctuations on the slope also do not give any conclusive results, neither visual shifting nor polynomial fitting help to find the time delay.

5.2.2. SDSS J1206+4332

In Figure 8 we show the light curve of SDSS J1206+4332. We see clear long variabilities for both the A and B light curves. The variabilities are 100–150 days long, so the gaps in the sampling do not strongly influence the precision of the time delay estimation. The observed variabilities, consisting of bumps, allow for measurement of the time delay for SDSS J1206+4332, as detailed in section 6.
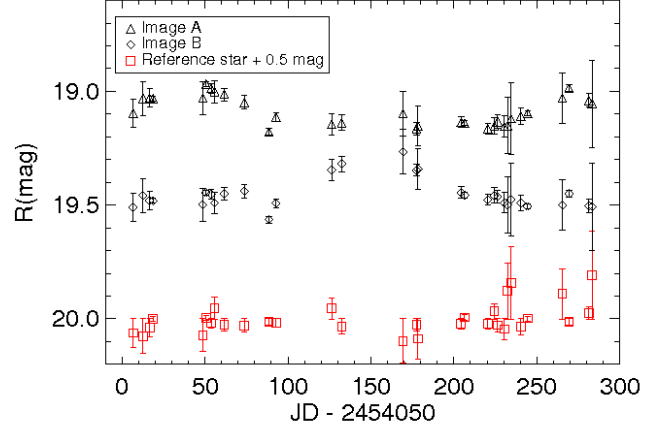

Fig. 8. R-band light curves of SDSS J1206+4332. Magnitude variabilities are seen in both light curves A (diamonds) and B (triangles) as bumps. The reference star is plotted with red squares.

6. Time delay of SDSS J1206+4332

From the geometry of the system SDSS J1206+4332 (see Figure 3) we anticipate that the A image is leading since it is farther from the centre of the main lensing galaxy. Thus, we predict that any intrinsic quasar variabilities should appear first in the A image. From the mass modeling we know also that the time delay for this system is ≥50 days (see Section 8). We apply these constraints when measuring the time delay from the light curves.
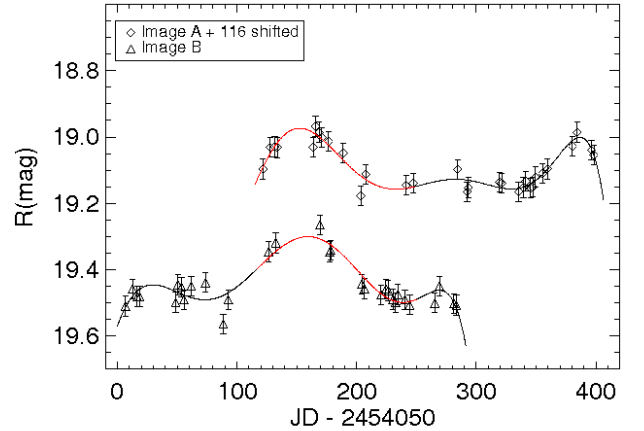

Fig. 9. R-band light curves of SDSS J1206+4332. Magnitude variabilities are seen in both light curves A (diamonds) and B (triangles) as bumps. The A light curve is shifted in time by 115 days. The red line indicates the intervals used for cross correlation.

The simplest form of such a measurement is visual shifting. Knowing that the variability has to appear first in the image A and then at least 50 days later in the image B we can associate the bump at the beginning of the A light curve centreed at ~50 days with the bump in the B light curve centreed at ~150 days.

A more quantitative measurement of a time delay is obtained by polynomial fitting. We fitted 7th order polynomials to both light curves using minimum χ^2. In Figure 9 we show the two polynomials (solid lines). We have marked in red the parts of the polynomials which were used for calculating the time delay. In
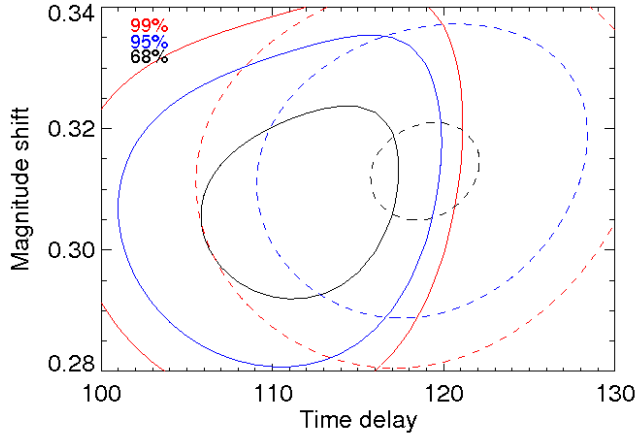
Fig. 10. Results of cross correlation between data on one image and fitted polynomial fitted to light curve of second image. Solid lines represents cross correlation between the A data and the polynomial fitted to B data; dashed lines are representing cross correlation between the B data and a polynomial fitted to the A data.

Fig. 11. Microlensing of SDSS J1206+4332. **Top:** Time-delay shifted light curves, with the A image offset by 0.32 mag and 115 days. **Bottom:** Difference between linearly interpolated A image and B image.

order to calculate the time delay we have shifted the A polynomial in time and magnitude to fit it to the B data points and the B polynomial was shifted in time and magnitude to fit it to A data points. For each shift of the polynomials the goodness of fit was calculated. The results of these fits are presented in Figure 10. For magnitude shift, $B - A = 0.31$ mag the average of the two time delay estimations is 116^{+6}_{-7} days, where errors are uncertainties of the two values of the time delay combined in quadrature. Based on our modeling (G1 – SIE and G3 – SIS) (see Section 8) and using the measured time delay ($\Delta\tau = 116^{+6}_{-7}$ days) we find a Hubble constant of 73^{+3}_{-4} km s^{-1} Mpc^{-1}.

7. Microlensing

Chang & Refsdal (1979) predicted that in lensed quasar systems the light path should be affected by stars in the lensing galaxy. Moving compact objects in the lensing galaxy can cause spectral changes, brightness variability and, in the case of multiple images, flux-ratio anomalies in the lensed quasar.

The images of a lensed quasar may vary due to intrinsic quasar brightness changes and/or microlensing. Microlensing affects the light paths of each image differently (in the simplest case only one path is affected) whereas the intrinsic variations show up in all the images but at different times due to the time delay. Therefore, one can isolate the microlensing signal by simply calculating the difference between two light curves.

If we shift one of the light curves in magnitude (by the magnitude difference between light curves) and in time (by the time delay) and subtract it from the other quasar counterpart light curve the remaining variation in the light curve difference should not belong intrinsically to the quasar but rather to microlensing.

Our previous study (Paraficz et al. 2006) showed that microlensing variabiliy can be detected in this way. The monitoring program presented in this paper was designed to be sensitive to such microlensing signals. The only limitation are S/N and gaps in the light curve due to bad weather conditions. In Figures 11–15 we present the result of a microlensing variability analysis for our observed targets.

The top plots present the quasar image lightcurves, with one of the images being shifted in time (by the theoretically pre-
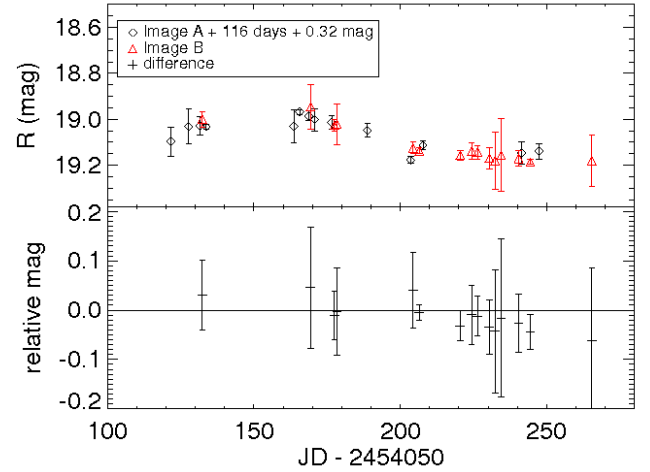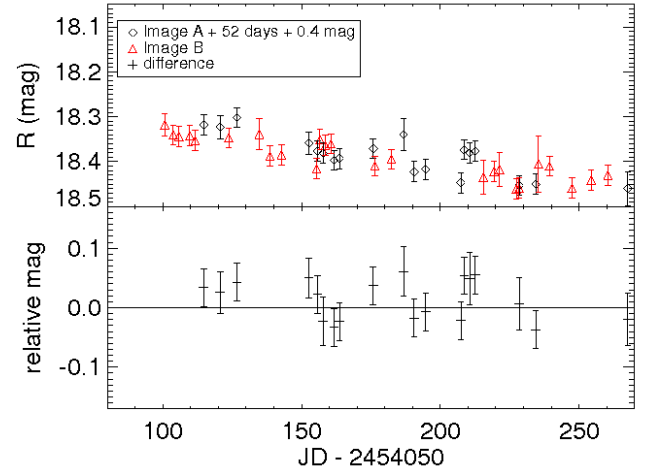

Fig. 12. Microlensing of SDSS J1001+5027. **Top:** Time-delay shifted light curves, with the A image offset by 0.4 mag and 52 days. **Bottom:** Difference between linearly interpolated A image and B image.

dicted or, if available, the measured time delay) and in magnitude (by the average magnitude difference between the images). The lower panels show the light curve differences. The difference is calculated between a linearly interpolated B light curve and the A data points. In Figures 11–15 we see that there is no signal stronger than 0.1 mag which is $\sim 2\,\sigma$. We therefore conclude that we did not detect any significant microlensing event in any of the systems during our monitoring program.

8. Modeling

8.1. Analytical modeling

In principle, one can calculate the Hubble constant from the time delay of a gravitationally lensed system, but there is one major obstacle, namely the mass-sheet degeneracy (Falco et al. 1985). This degeneracy is between the Hubble constant and the radial density profiles of the lens (Wucknitz & Refsdal 2001) and its angular structure (Freedman et al. 2001). Summarizing, different mass profiles give different results on the Hubble constant
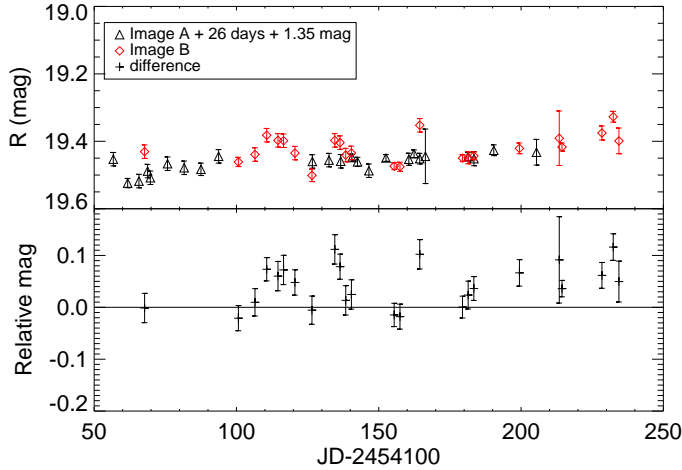
Fig. 13. Microlensing of SDSS J1335+0118. **Top:** Time-delay shifted light curves, with the A image offset by 1.35 mag and 26 days. **Bottom:** Difference between linearly interpolated A image and B image.
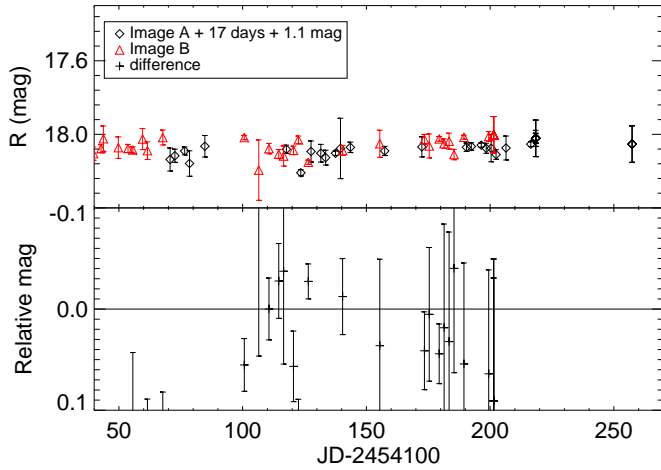

Fig. 14. Microlensing of SDSS J1353+1138. **Top:** Time-delay shifted light curves, with the A image offset by 1.1 mag and 17 days. **Bottom:** Difference between linearly interpolated A image and B image.
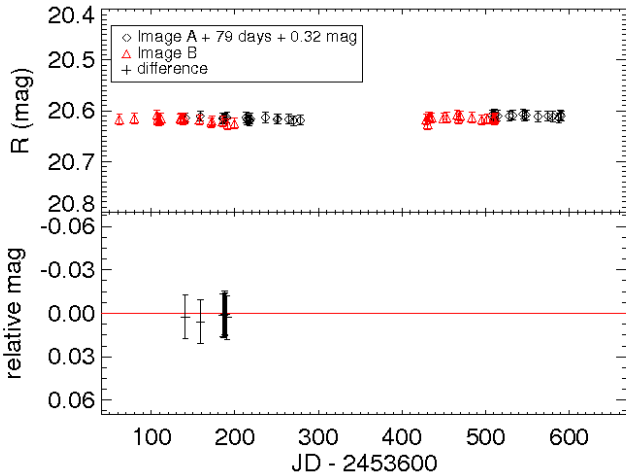

Fig. 15. Microlensing of SDSS J0903+5028. **Top:** Time-delay shifted light curves, with the A image offset by 0.32 mag and 79 days. **Bottom:** Difference between linearly interpolated A image and B image.

without changing the lensing configuration. To break this degeneracy we need to have information about the mass profile, e.g., through the velocity dispersion (Romanowsky & Kochanek 1999). For our systems we do not know which lens model is the correct one, but fortunately in many cases a lens can be quite well modeled using a fairly simple mass model like SIE (Singular Isothermal Ellipsoid) (Kormann et al. 1994) or NFW (Navarro-Frank-White) (Golse & Kneib 2002).

In this paper, for the analytical modeling, we have modeled all our systems using singular isothermal potentials. We used those models because of their simplicity and because they agree with the physical properties of many observed lenses (Kochanek 1993; Rusin et al. 2003; Koopmans et al. 2006).

In the analytical modeling we have the positions of the two images as constraints and as free parameters we have the lens velocity dispersion, σ_0 and the ellipticity, ϵ. We also have two fixed parameters, the position angle, θ_ϵ and the position of the lens galaxy. The number of degrees of freedom is 0, thus we can look for the one model which perfectly fits the data. The positions of the images and lens are visible on the decovolved images (see Figure 3). The position angle of the lenses can be roughly estimated from analysis of the deconvoled images, as the mass profile of a lens tends to align to its visible component (Keeton et al. 1998). We allow this constraint to vary within $45°$. We have not used flux ratios as constraints because of the possible influence of reddening by dust (Elíasdóttir et al. 2006), microlensing (Paraficz et al. 2006) or small-scale structure in the lens potential (Dalal & Kochanek 2002).

The ellipticity used here is defined as $\epsilon = (a^2 - b^2)/(a^2 + b^2)$, where a and b are the major and minor axis. The position angle corresponds to the direction of the semi-major axis of the isopotential counted east of north. The modeling has been performed using the LENSTOOL software package available at http://www.oamp.fr/cosmology/lenstool/ (Jullo et al. 2007). LENSTOOL is a software created for modelling strong lensing systems with parametric methods which chooses models using the Bayesian evidence. In all models we set the Hubble constant to be $H_0 = 73$ km s^{-1} Mpc^{-1}.

8.1.1. SDSS J0903+5028

We have fitted the two simple models, SIS (Singular Isothermal Sphere) and SIE (Singular Isothermal Ellipsoid) to the lensing galaxy of SDSS J0903+5028. We have assumed that only one galaxy, the central one, influences the quasar light, even though other galaxies are visible to the north and south of the images (see Figure 16). The lensing images of the quasar are not collinear with the central galaxy which indicates that there is a quadruple moment in the potential. This moment can come from the tidal effect of the nearby galaxies or may be due to elongation of the central galaxy. Because of the degeneracy we are not able to distinguish which one of the possibilities is true, thus we use one lens, an SIE model which accurately predicts image positions. In Table 2 we summarize the results of the SDSS J0903+5028 modeling where the central single lens is an SIE. Based on this model, the predicted time delay for the system is 79.4 days. The uncertainty in this value is entirely dominated by systematic modeling uncertainties.

8.1.2. SDSS J1001+5027

The lens of SDSS J1001+5027 consists of two galaxies (see Figure 3) which according Oguri et al. (2005) are at similar red-
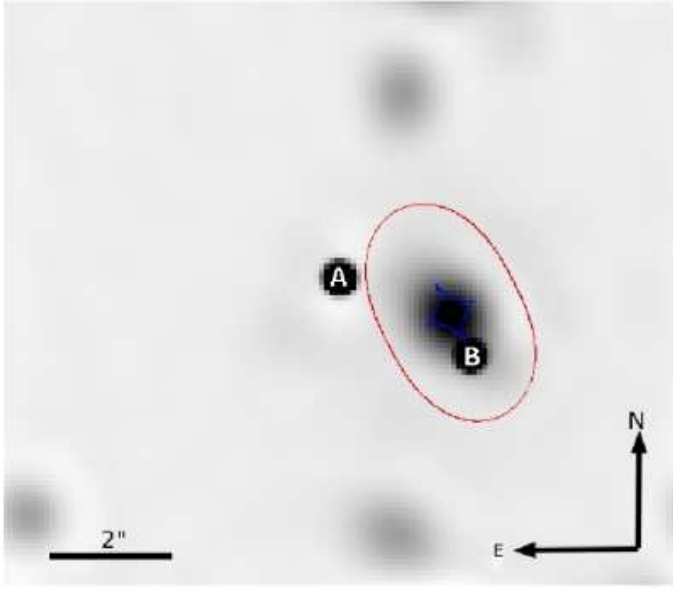
Fig. 16. Lens model of SDSS J0903+5028. The figure shows an image of the system with over-plotted results of lens modeling. Blue and red lines represent critical and caustic lines, respectively.

#	Type	x	y	σ_0	ϵ	θ_ϵ	$\Delta\tau$
		arcsec	arcsec	km s^{-1}			days
G	SIE	1.99	-0.70	264.6	0.49	27°	79.4

Table 2. Lens model of SDSS J0903+5028. Modeled parameters are galaxy position, x, y, lens velocity dispersion, σ_0, ellipticity, ϵ, position angle, θ_ϵ and time delay, $\Delta\tau$.

shifts $0.2 < z < 0.5$. For our modeling we fix both lensing galaxies at redshift 0.3.

We have created two possible models of the lens environment of SDSS J1001+5027. In the first one the system has only one galaxy with elongated SIE mass profile. This model is able to ray-trace the position of the quasar images. From Figure 17 we also see that the position angle, P.A. of the model is consistent with the light distribution of the main galaxy but it is also in the direction of the other galaxy. This leads to the conclusion that the quadruple moment might come from the second galaxy rather then from the elongation of the main one. In the second version of the lens model we have set both gravitational lenses as Singular Isothermal Spheres, SIS. This model also reproduces the position of the quasar images and gives a sensible result of the galaxy velocity dispersions being 223 km s^{-1} for main lens (G1) and 159 km s^{-1} for G2. The results from both models are presented in Figure 17 and summarized in Table 3. The predicted time delay of the system is 34 days based on the SIE model and 52 days based on the double SIS model.

#	Type	x	y	σ_0	ϵ	θ_ϵ	$\Delta\tau$
		arcsec	arcsec	km s^{-1}			days
G1	SIE	1.749	0.861	258	0.23	11°	52
G1	SIS	1.749	0.861	223	0	0	34
G2	SIS	1.629	−0.588	159	0	0	34

Table 3. Lens model of SDSS J1001+5027. Parameters are as in Table 2.

Fig. 17. Lens model of SDSS J1001+5027. The figure shows an image of the system with over-plotted results of lens modeling. Blue and red lines represent critical and caustic lines, respectively. Top plot present the single SIE lens model and the bottom plot presents the two SIS lens models.

8.1.3. SDSS J1206+4332

We have fitted SIS and SIE to the main lensing galaxy of the SDSS J1206+4332. We have assumed that the only galaxy which influences the quasar light is the central galaxy G1 (see Figure 3). Unfortunately we come to the same conclusions as (Oguri et al. 2005) that neither of these mass models gives physically realistic results. The system seems to be more complicated, so presumably the other galaxies seen in vicinity of the system may play a role. A model of the main galaxy G1 (SIE) and G2 (SIS) does not give any physical solutions either, which is expected since the redshift of G2 is predicted to be rather small.

It appears that the third galaxy lying ∼ 3″ north of the system (see Figure 3) has a strong influence on the system geometry. If we assume our model to be two lensing galaxies with one of them being G1 (SIE) and the other G3 (SIS) it is possible to reproduce the positions of the images. The results of that final fitting are summarized in Table 4. Based on this model, the predicted time delay of the system is 112.5 days which is in agreement with our measurement of 116^{+6}_{-7} days (see section 6).
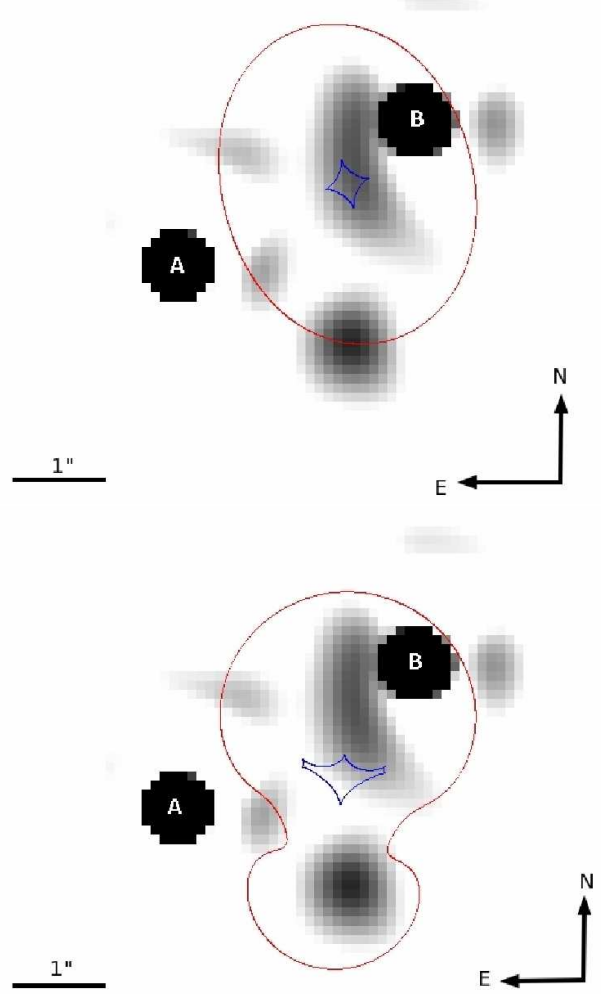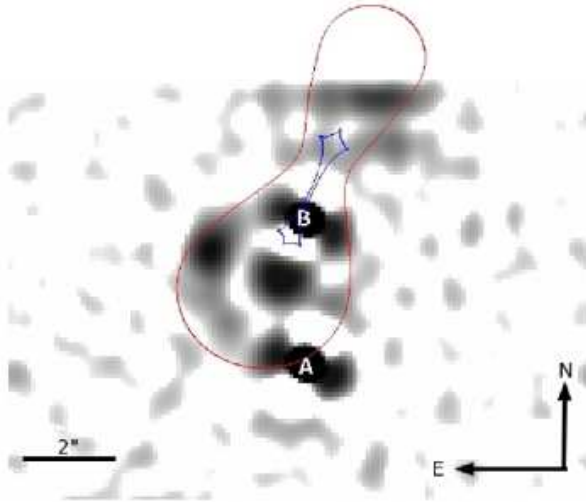
Fig. 18. Lens model of SDSS J1206+4332. The figure shows an image of the system with over-plotted results of lens modeling. Blue and red lines represent critical and caustic lines respectively.

#	Type	x arcsec	y arcsec	σ_0 km s^{-1}	ϵ	θ_ϵ	$\Delta\tau$ days
G1	SIE	−0.66	1.75	347.5	0.1	−2°	112.5
G3	SIS	1.32	5.9	279.5	0	-	112.5

Table 4. Lens model of SDSS J1206+4332. Parameters are as in Table 2

Fig. 19. Mass model of SDSS J1335+0118. Figure shows an image of the system with over-plotted results of lens modeling. Blue and red lines represent critical and caustic lines, respectively.

8.1.4. SDSS J1335+0118

The system has one lensing galaxy, at redshift $z = 0.5$, which we have modeled as an SIE. The lensing galaxy is barely visible in our images, hence the position of the galaxy was taken from Oguri et al. (2004). According to observations made by Oguri et al. (2004) with Keck, the lensing galaxy is misaligned with the QSO images which indicates the existence of external shear or elongation of the lensing galaxy. A model with an SIE lens accurately predicts the image position and gives plausible galaxy parameters. The model details are summarized in Table 5. The estimated time delay of the system is 26.2 days which is in agreement with previous studies.
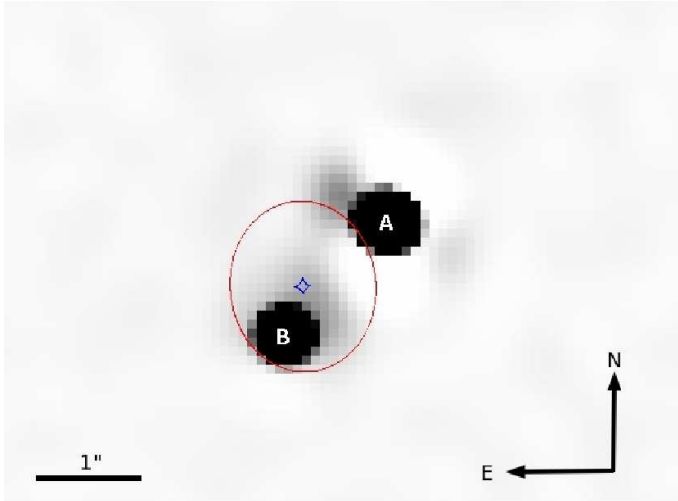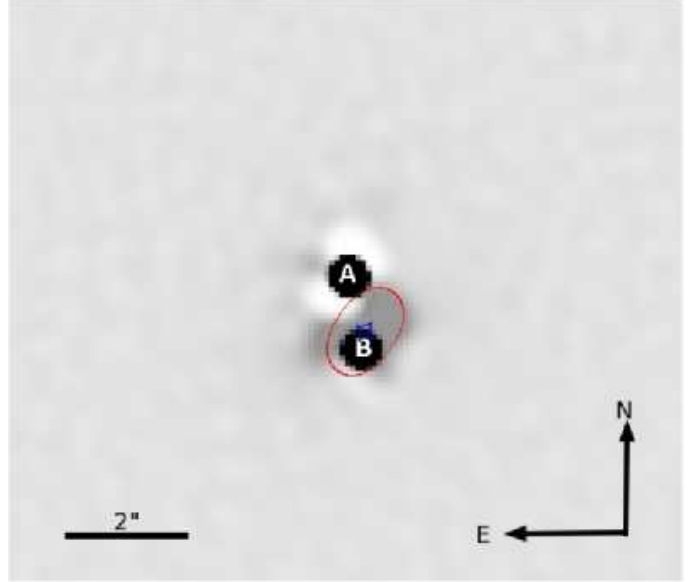

Fig. 20. Mass model of SDSS J1353+1138. Figure shows an image of the system with over-plotted results of lens modeling. Blue and red lines represent critical and caustic lines, respectively.

#	Type	x arcsec	y arcsec	σ_0 km s^{-1}	ϵ	θ_ϵ	$\Delta\tau$ days
G	SIE	−0.786	−0.649	218	0.16	−5°	26.2

Table 5. Lens model of SDSS J1335+0118. Parameters are as in Table 2

8.1.5. SDSS J1353+1138

SDSS J1353+1138 has a centrally aligned lensing galaxy and the B image very close to the galaxy centre. There are no other close-by galaxies; thus the lens can be modeled with a simple SIE. The predicted time delay for that system is 17 days (see Table 6) which is in agreement with previous studies.

#	Type	x arcsec	y arcsec	σ_0 km s^{-1}	ϵ	θ_ϵ	$\Delta\tau$ days
G	SIE	−0.25	−1.04	177	0.46	35°	17.2

Table 6. Lens model of SDSS J1353+1138. Parameters are as in Table 2

8.2. Non-parametric modeling

We have also modeled our systems based on a non-parametric method proposed by Saha & Williams (1997) using the publicly available code PixeLens (Saha & Williams 2004).

PixeLens reconstructs a pixelated mass map of the lens by implementing Bayesian statistics. It generates numerous lens models which fit the lens system geometry. There are two major advantages of using this method. First, it allows to explore a wide range of models not restricted with parameters, which circumvents the non-uniqueness problem of lens modeling. Second, it provides an estimate of the systematic errors on the modeled time delay which is not possible to get when using analytical methods. Our purpose of using it is to check the robustness of our time delay estimations, i.e. we want to know whether the two approaches, analytical and pixeleted, give consistent results for the time delays. PixeLens generates mod-
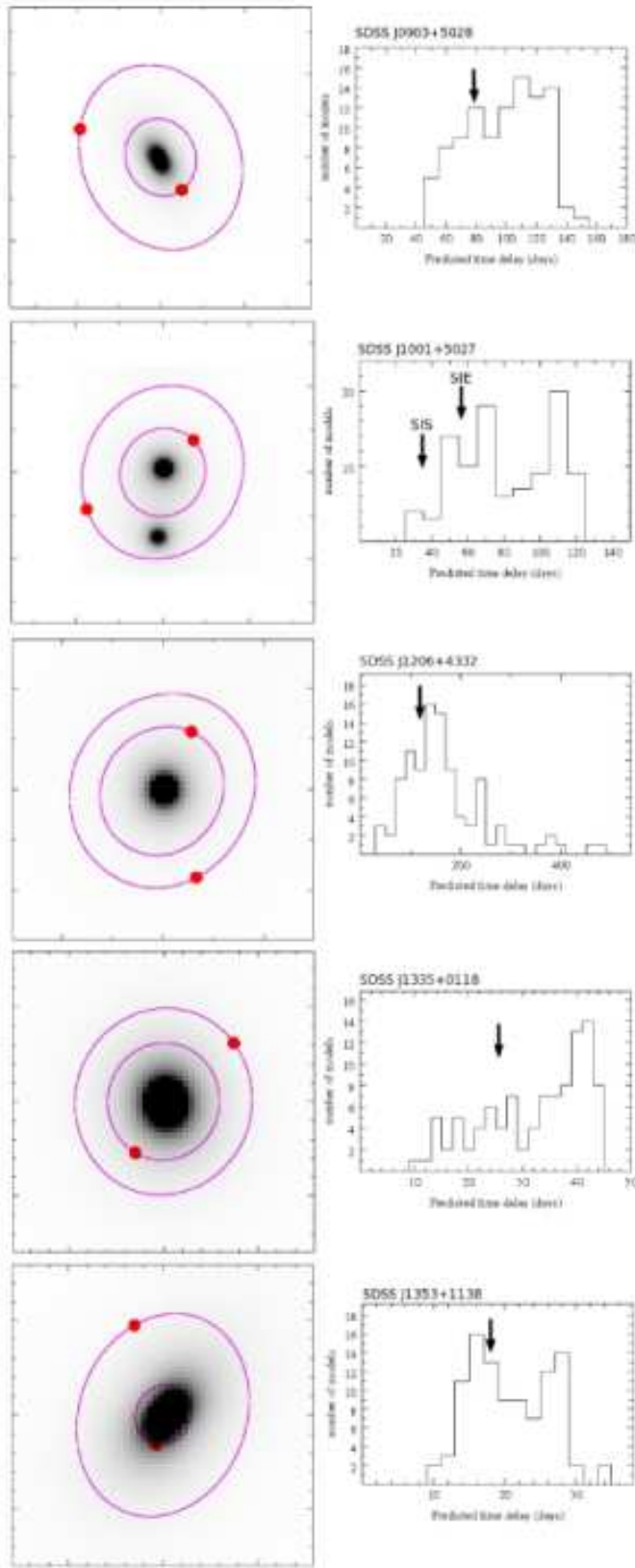
els which reproduce the exact position of lensing images and aligned within 45° of the visible lens P.A. All our systems were modeled assuming existence of external shear and all of them, except SDSS J1206+4332, were modeled as symmetric. For each system we generated 300 lens models which were used to estimate the average and median time delay and their model uncertainties. The modeling results of the 5 gravitationally lensed QSOs with PixeLens are summarized in Table 7. Figure 21 shows the potentials and time delays of the 5 systems modeled with pixelated method. On the left side we see potential contours modeled by PixeLens which are over-plotted on the mass map created in analytical modeling. On the right are histograms of the time delays generated for each system by the 300 lens models.

We see that the lens potentials of the PixeLens correspond to the analytical models and from the Table 7 we see that the estimated time delay values from analytical modeling lie within error bars of the PixeLens time delays. This is reassuring and gives confidence in our approach. We note also that the analytically obtained time delays are systematically lower than the average values obtained using PixeLens by 20–50%.

#	Analytical Model	PixeLens average	PixeLens median
0903+5028	79.4	98±21	101^{+9}_{-12}
1001+5027	52	81±23	76^{+14}_{-9}
1206+4332	113	173±64	152^{+41}_{-21}
1335+0118	26	32±8	35^{+2}_{-6}
1353+1138	17	21±5	20^{+3}_{-2}

Table 7. Summary of modeled time delays of the five lensed quasars. Two different modeling methods are compared. For the pixelated method we generate 300 lens models for each system which are used to estimate the average and median time delay and their error bars. We see that the estimated time delays from analytical modeling are consistent with he PixeLens time delays.

9. Simultanous modeling

The Hubble constant estimated from time delay measurements is model dependent, as illustrated above. Different models give a different Hubble constant and measuring the time delay with high precision does not resolve that issue. One way of dealing with this problem is to generate a large number of models of many lenses and create a distribution of possible values for the Hubble constant based on these models. Thus, we use the pixelated method for several gravitationally lensed systems constraining them to have the same shared value of H_0. Simultaneous modeling has been done in the past by e.g. Saha et al. (2006) – with 10 lenses and Coles (2008) – with 11 lenses.

Figure 22 shows the result of the simultaneous modeling of 5 systems with time delays obtained at the NOT. These are RX J0911+055 (Hjorth et al. 2002), SBS B1520+530, (Burud et al. 2002b), B1600+434 (Burud et al. 2000) and J0951+263 (Jakobsson et al. 2005) and the time delay of SDSS J1206+4332 reported in this paper. On the histogram the results of our simultaneous modeling of the 5 QSOs are presented. For each object 100 lens models were created. The Hubble constant estimated using this method is $H_0 = 61.5^{+8}_{-4}$ km s^{-1} Mpc^{-1}.

Fig. 21. The modeling results of the five lensed quasars. On the left side we see potential contours modeled by PixeLens which are over-plotted on the mass map created in analytical modeling. On the right the are time delay histograms generated for each system by the 300 suitable lens models, arrows indicate the time delays estimated from analytical modeling. We see that the potentials of the PixeLens correspond quite well to the analytical models
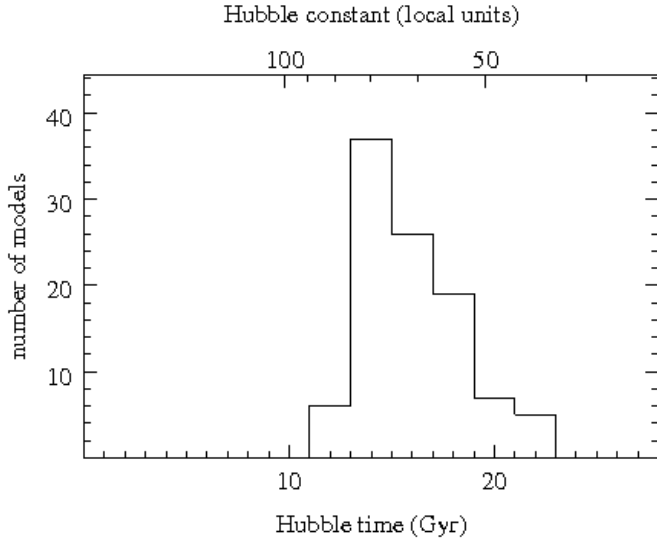
Fig. 22. The result of the simultaneous modeling, it is a histogram created from the modeling of the 5 QSOs monitored at the NOT for each of them 100 lens models were created, the Hubble constant estimated using this method is $H_0 = 61.5^{+8}_{-4}$ km s^{-1} Mpc^{-1}.

10. Discussion

We have estimated the time delay of the SDSS J1206+4332 to be $\Delta\tau = 116^{+6}_{-7}$ based on a 280-day long monitoring campaign at the Nordic Optical Telescope. This shows the feasibility of measuring time delays from campaigns not much longer than the time delay itself. To model the system, we first assumed a single lensing galaxy modeled with the Singular Isothermal Ellipsoid (SIE), but were unable to reproduce the image positions. By adding to the lens model the G2 and G3 galaxies we found that the influence of the G2 galaxy is negligible due to its small redshift but the G3 galaxy has a major impact on the system's geometry. A lens model with two galaxies, where the main one is a SIE and the second is a SIS, predicts the image positions very well. Thus this model resulted in a Hubble constant of 73^{+3}_{-4} km s^{-1} Mpc^{-1} assuming $\Omega_m = 0.3$ and $\Omega_\Lambda = 0.7$.

Lack of short-term variability in the other monitored systems (SDSSJ 0903, SDSS J1001+5027, SDSS J1353+1138, SDSS J1335+0118) meant that we did not succeed in measuring their time delays. From the quasar studies of Fohlmeister et al. (2008), Vuissoz et al (2007), Koopmans et al. (2000) and many others we see that during the 200–300 days of a quasar monitoring a quasar might be at the quiet stage or at the slow increase or decrease. Thus, despite our success in measuring the time delay of SDSS J1206+4332, it appears that monitoring substantially longer than the predicted time delay of a given system will be unavoidable in many cases.

We have modeled all five systems using both analytical and pixelated methods. Using the predicted time delays we have shown that none of the systems exhibited significant microlensing variability during the observing campaign.

We have also performed simultaneous pixelated modeling with a common Hubble constant of five lenses for which time delays were measured at the NOT. The estimated Hubble constant from this analysis is $H_0 = 61.5^{+8}_{-4}$ km s^{-1} Mpc^{-1}.

References

Burud, I., Hjorth, J., Jaunsen, A. O., et al. 2000, ApJ, 544,117
Burud, I., Courbin, F., Magain, P., et al. 2002a, A&A, 383, 71
Burud, I., Hjorth, J., Courbin, F., et al. 2002b, A&A, 391, 481
Chang, K. & Refsdal, S. 1979, Nature, 282, 561
Coles, J. 2008, ApJ, 679, 17
Dalal, N. & Kochanek, C. S. 2002 ApJ, 572, 25
Eigenbrod, A., Courbin, F., Dye, S., et al. 2006, A&A, 451, 747
Eigenbrod, A., Courbin, F., Meylan, G., et al. 2006, A&A, 451, 759
Elíasdóttir, ., Hjorth, J., Toft, S., et al. 2006, ApJ, 166, 443
Falco, E., Gorenstein, M., M. V. & Shapiro, I. L. 1985, ApJ, 289, L1
Faure, C., Courbin, F., Kneib, J. P., et al. 2002, A&A, 386, 69
Fohlmeister, J., Kochanek, C. S., Falco, E. E., et al. 2008, ApJ, 676, 761
Freedman, W. L., Madore, B. F., Gibson, B. K. 2001, ApJ, 553, 47
Golse, G. & Kneib, J. P. 2002, A&A, 390, 821
Hjorth, J., Burud, I., Jausen, A. O., et al. 2002, ApJ, 572, 11
Inada, N., Oguri, M., Becker, R. H., et al. 2006, AJ, 131, 1934
Jakobsson, P., Hjorth, J., Burud, I., et al. 2005, A&A, 431, 103
Johnston, D. E., Richards, G. T., Frieman J. A., et al. 2003, ApJ, 131, 1934
Jullo, E., Kneib, J. P., Limousin, M., et. al. 2007, NJPh, 9, 447
Keeton, C., R. 2001, ApJ submitted (astro-ph/0102340)
Keeton, C. R., Kochanek, C. S. & Falco, E. E. 1998, ApJ, 509, 561
Kochanek, C. S. 1993, ApJ, 419, 12
Koopmans, L. V. E., de Bruyn, A. G., Xanthopoulos, E., et al. 2000, A&A, 356, 391
Koopmans, L. V. E., Treu, T., Bolton, A. S., et al. 2006 ApJ, 649, 599
Kormann, R., Schneider, P. & Bartelmann, M. 1994, A&A, 284, 285
Magain, P., Courbin F & Sohy, S. 1998, ApJ, 494, 472
Oguri, M., Inada, N.,Castander, F. J., et al. 2004, PASJ, 56, 399
Oguri, M., Inada, N., Hennawi, J. F., et al. 2005, ApJ, 622, 106
Oguri, M. 2007, ApJ, 660, 1
Paczyński, B. 1986, ApJ, 301, 503
Paraficz, D., Hjorth, J., Burud, I., et al. 2006, A&A, 455, 1
Refsdal 1964, MNRAS, 128, 307
Romanowsky, A. J. & Kochanek, C. S.,1999, ApJ, 516, 18
Rusin, D., Kochanek, C. S. & Keeton, C. R. 2003, ApJ, 595, 29
Saha P. & Williams L. L. R. 1997, MNRAS, 292, 148
Saha P. & Williams L. L. R. 2004, AJ, 127, 2604
Saha, P., Coles, J., Macció, A. V., et al. 2006, ApJ, 650, 17
Schild, R. 1996, AAS, 189, 2702
Webb, W. & Malkan, M. 2000, ApJ, 540, 652
Wold, M., Brotherton, M. S. & Shang, Z. 2007, MNRAS, 375, 989
Wucknitz, O., Refsdal, S. 2001, ASPC, 237, 157
Wyithe, J. S. B., & Turner, E. L. 2001, MNRAS, 320, 21
de Vries, W. H., Becker, R. H. & White, R. L. 2003, AJ, 126, 1217
de Vries, W. H., Becker, R. H. & White, R. L. 2006 ASPC, 360, 29
Vuissoz, C., Courbin, F., Sluse D., et al. 2007, A&A, 464, 845

Table.3. Photometry of two images of SDSS J0903+5028 quasar.

$Rmag_A$	$Rmag_B$	JD
20.304195	20.616799	061.73267
20.300746	20.615271	079.76126
20.305079	20.608090	106.76752
20.304733	20.616682	107.72829
20.306558	20.619706	108.77146
20.304743	20.618817	109.75729
20.303631	20.615568	111.70990
20.302910	20.616263	134.49363
20.307745	20.615292	135.60198
20.305574	20.617903	137.56633
20.309453	20.618127	138.65267
20.305457	20.614339	139.65707
20.302961	20.618014	157.56273
20.306617	20.623384	171.54778
20.305926	20.620051	172.58139
20.306603	20.620899	185.40632
20.309605	20.626972	191.46353
20.308627	20.625028	199.52655
20.298319	20.617214	428.69561
20.301808	20.627140	430.74676
20.296764	20.612383	431.69420
20.298253	20.612072	432.73686
20.299821	20.614314	435.74226
20.300707	20.614775	449.59337
20.299069	20.613606	453.71216
20.296104	20.608069	465.70068
20.300696	20.615813	467.67382
20.298169	20.609918	469.74747
20.301014	20.613560	483.76553
20.300752	20.617619	495.56600
20.301731	20.615859	501.74698
20.303775	20.616146	508.74511

Table.3. Photometry of two images of SDSS J1001+5027 quasar and a reference star.

$Rmag_A$	$Rmag_B$	$Rmag_{ref}$	Err Rmag	JD
18.308300	17.916424	19.959659	0.124381	050.69800
18.323450	17.937721	19.929005	0.034650	062.73200
18.307941	17.943148	19.933155	0.049381	068.69100
18.277621	17.921927	————	0.022007	074.71047
18.317622	17.978474	19.906741	0.046542	100.66100
18.340800	17.996533	19.931855	0.028322	103.73100
18.343249	18.001368	19.906263	0.018813	105.76800
18.342268	18.016725	20.028774	0.028204	109.72400
18.353127	18.013164	19.943019	0.147739	111.65300
18.346979	17.990860	19.911710	0.010532	123.78600
18.339169	17.959495	————	0.034687	134.75378
18.387632	18.042124	19.966310	0.011901	138.58600
18.385108	18.037049	19.931430	0.012798	142.76500
18.415253	18.066928	19.936043	0.018701	155.43300
18.350806	17.993212	————	0.027625	156.58644
18.363621	18.000546	————	0.020099	158.59506
18.360164	17.996483	————	0.010037	160.60051
18.409971	18.072709	19.948912	0.013566	176.41200
18.394950	18.070155	19.918187	0.010659	182.41100
18.435319	18.079750	————	0.037845	215.53896
18.421549	18.055671	19.896153	0.010842	219.38300
18.417204	18.075555	————	0.037845	221.36005
18.460061	18.094696	19.930324	0.038369	227.41000
18.459076	18.113779	19.938801	0.093712	228.37800
18.405639	18.072108	————	0.063487	235.38689
18.409954	18.081878	————	0.018256	239.39029
18.459080	18.126627	19.937951	0.010008	247.42200
18.440717	18.107298	19.904796	0.010067	254.39000
18.429906	18.072435	————	0.091177	260.41507
18.487492	18.093200	————	0.066955	276.40500

Table.3. Photometry of two images of SDSS J1206+4332 quasar and a reference star.

$Rmag_A$	$Rmag_B$	$Rmag_{ref}$	Err Rmag	JD
19.509589	19.096939	19.562536	0.062694	006.72319
19.458226	19.031157	19.575507	0.075527	012.73698
19.480679	19.029276	19.539772	0.040385	016.66442
19.481074	19.031575	19.501510	0.010037	018.69594
19.498675	19.030665	19.572343	0.072392	048.69698
19.445953	18.967233	19.497185	0.010581	050.66706
19.452695	18.985873	19.519436	0.021286	053.73665
19.490599	19.001164	19.453006	0.048676	055.77248
19.449798	19.013616	19.526555	0.027773	061.65876
19.438714	19.048370	19.529403	0.030448	073.79091
19.563541	19.177637	19.512119	0.015220	088.59046
19.490950	19.112350	19.516885	0.019072	092.76935
19.345731	19.145619	19.454153	0.047554	126.41778
19.318989	19.138562	19.532942	0.033810	132.41905
19.265193	19.097541	19.597853	0.097722	169.38858
19.346323	19.165073	19.525828	0.027097	177.49348
19.341391	19.152732	19.587948	0.087875	178.38291
19.444082	19.135932	19.522717	0.024232	204.39591
19.456705	19.139128	19.494133	0.011932	206.47791
19.476497	19.165282	19.520598	0.022319	220.46142
19.458248	19.152088	19.467670	0.034457	224.38148
19.463009	19.133444	19.528405	0.029507	226.41176
19.489138	19.153896	19.544838	0.045311	230.41777
19.499540	19.151204	19.377492	0.123557	232.41145
19.475140	19.120366	19.341953	0.159005	234.46066
19.490768	19.109479	19.534108	0.034926	240.41984
19.506084	19.096243	19.498606	0.010205	244.40898
19.500106	19.028428	19.390230	0.110865	265.40616
19.449340	18.985593	19.512254	0.015322	269.39189
19.502726	19.039390	19.473984	0.028473	281.37866
19.507411	19.054861	19.307993	0.192910	283.37888

Table.3. Photometry of two images of SDSS J1335+1138 quasar and a reference star.

$Rmag_A$	$Rmag_B$	$Rmag_{ref}$	Err Rmag	JD
18.103033	19.366769	———	0.020000	30.724810
18.173849	19.445618	———	0.020000	35.773720
18.168048	19.507642	19.811958	0.017249	39.739070
18.138333	19.480296	19.827976	0.010191	42.774090
18.158132	19.434327	———	0.020000	43.732740
18.116399	19.338482	———	0.020000	49.774310
18.128543	19.508473	19.835769	0.013971	55.622420
18.132991	19.461828	———	0.020000	61.534550
18.094535	19.430734	———	0.020000	67.730140
18.109781	19.461155	19.816665	0.013688	100.67228
18.105817	19.439126	———	0.020000	106.51100
18.109180	19.381934	———	0.020000	110.62587
18.098207	19.397216	———	0.020000	114.58660
18.110809	19.398308	———	0.020000	116.54903
18.137283	19.435018	———	0.020000	120.53586
18.099405	19.501067	19.810479	0.018473	126.52229
18.103190	19.397234	———	0.020000	134.55204
18.086870	19.403923	———	0.020000	136.39267
18.101415	19.440893	———	0.020000	138.40052
18.094541	19.434533	———	0.020000	140.38453
18.095505	19.473765	19.828225	0.010241	155.41550
18.101533	19.475559	19.835056	0.013482	157.45223
18.076486	19.352538	———	0.020000	164.41317
18.082410	19.449831	19.824963	0.010035	179.41976
18.086675	19.448914	19.826855	0.017975	181.40853
18.088464	19.443357	19.840949	0.011272	183.41002
18.063292	19.420842	19.820810	0.015805	199.42655
18.017446	19.390862	19.838252	0.080799	213.41659
18.052497	19.417072	19.745833	0.012022	214.39304
18.045362	19.375354	19.832686	0.020918	228.41725
18.069432	19.327107	19.844385	0.016030	232.38603
18.057617	19.398826	19.838541	0.038127	234.37637

Table.3. Photometry of two images of SDSS J1353+0118 quasar and a reference star.

$Rmag_A$	$Rmag_B$	$Rmag_{ref}$	Err Rmag	JD
17.058143	18.078725	———	0.062755	035.76942
17.027750	18.105148	18.374450	0.035975	039.74420
17.004627	18.077990	18.428243	0.021679	042.77780
16.968521	18.023901	———	0.069111	043.72839
17.036874	18.072364	———	0.058642	049.77080
17.036695	18.077008	18.429024	0.022376	053.68090
17.016458	18.085246	18.395050	0.017169	055.62640
16.990376	18.025689	———	0.057302	059.57378
17.058655	18.088771	———	0.048000	061.52997
16.964883	18.017243	———	0.040402	067.73733
16.981154	18.017522	18.415777	0.012076	100.67650
17.109052	18.194647	———	0.164170	106.51640
16.993320	18.077777	———	0.028363	110.62981
17.002714	18.107406	———	0.024942	114.59100
17.026681	18.117991	———	0.054771	116.55300
17.002861	18.087047	———	0.023093	120.53156
16.976714	18.029956	———	0.020771	122.53589
16.970766	18.151632	18.414655	0.011484	126.52910
16.990348	18.087793	———	0.027337	140.38854
16.968081	18.051361	18.336053	0.073636	155.42000
16.970249	18.026965	18.384892	0.026106	173.44620
16.966204	18.063215	18.344583	0.065195	175.39800
16.958724	18.024720	18.400829	0.012918	179.41520
16.975812	18.050705	18.385252	0.025774	181.40410
16.975648	18.037233	18.366688	0.043484	183.40570
17.009698	18.109882	———	0.028265	185.39787
16.974296	18.015906	18.404894	0.010812	189.42540
16.953534	18.011738	18.433626	0.026571	199.43070
16.921712	18.002514	———	0.099206	201.43826
16.950484	17.994469	18.491207	0.082805	213.42560
16.969916	18.041750	18.442072	0.034543	214.38850
16.963528	18.037533	18.444302	0.036684	216.42800
16.976914	18.056241	18.388224	0.023063	220.41840
16.946127	18.035193	18.394833	0.017347	228.42160
16.960770	18.070003	18.418786	0.013986	232.38040
16.961527	18.025517	18.410923	0.010181	234.37150
16.950683	18.015915	18.424231	0.018214	238.35420
16.953166	18.031116	———	0.070280	240.37300